Numerical simulation and experimental analysis of the sintered micro-parts using the powder injection molding process

Mohamed Lakdhar Sahli, Hamza Djoudi, Jean-Claude Gelin, Thierry Barriere, Mohamed Assoul

Numerical simulation and experimental analysis of the sintered micro-parts using the powder injection molding process

M. Sahli[1,2] · H. Djoudi[1] · J.-C. Gelin[1] · T. Barriere[1] · M. Assoul[1]

Abstract This paper discusses in detail the development of numerical simulations capable of simulating structural evolution and macroscopic deformation during a powder injection molding process. A sintering model based on elastic-visco-plastic constitutive equations was proposed, and the corresponding parameters such as sintering stress, bulk and shearing viscosities were identified from dilatometer experimental data. As a complement to this experimental study, a finite element simulation of the sintering operation was performed. The simulations were based on constitutive equations identified from specific experiments performed for each blend at different sintering heating rates and loadings. Finally, the numerical analyses, performed on the 3D micro-structured components, allow the numerical predictions to be compared with experimental results of sintering stage. They show that the FE simulation results have better agreement with the experimental ones at high temperatures.

The original version of this article was revised: Unfortunately, one of the co-author's family name was incorrect in the original online publication of this article. The correct family name should be: Barriere.

✉ M. Sahli
sahlisofiane2@yahoo.fr

[1] Applied Mechanics Department, CNRS, UMR 6174, Femto-ST Institute, 25030 Besançon cedex, France

[2] Mechanics Laboratory, Faculty of Engineering Sciences, University Mentouri, Constantine, Algeria

1 Introduction

In recent years, the miniaturization and manufacturing of micro-components have gained increasing attention in both industry and academia (Packianather et al. 2015; Bleyan et al. 2015; Packianather et al. 2013; Lebib et al. 1999). The microinjection molding processes is rapidly becoming one of the most promising fabrication technologies for the production of thermoplastic polymer micro-parts (He et al. 2016; Bricout et al. 2015; Han et al. 2016; Choi et al. 2015). Most of the applications are concentrated in the fields of micro-optics, micro-fluidics and medical instruments. The metal injection molding (MIM) is a manufacturing technology that combines the shaping efficiency of plastic injection molding with the capability of powder metallurgy for processing metal powders. This process permits to get net shape components with complex geometry from polymers combined with metals (Meng et al. 2011; Heaney et al. 2005; Fu et al. 2004). The MIM is used in several fields as automotive and aeronautics, data processing, electronics, etc. (Petzoldt 2008; Ruprecht et al. 2002). In this process, a custom-formulated mixture of an extremely fine metal powder and wax-polymer-based binders are initially blended into a moldable formulation. The binder transports the metal powder to fill out the desired geometry. The green component, which consists of two materials with a low cohesive force, cannot be used in this form for most applications because material properties such as strength and modulus are very low, thus it must be debound and sintered. In thermal debinding, the binder diffuses through the pores to the component external surfaces where it is removed as vapor. At the end of the thermal debinding, the component is considered brown and ready for sintering (German 1997; Raza et al. 2015; Contreras et al. 2009; Mukund et al. 2015). During sintering,

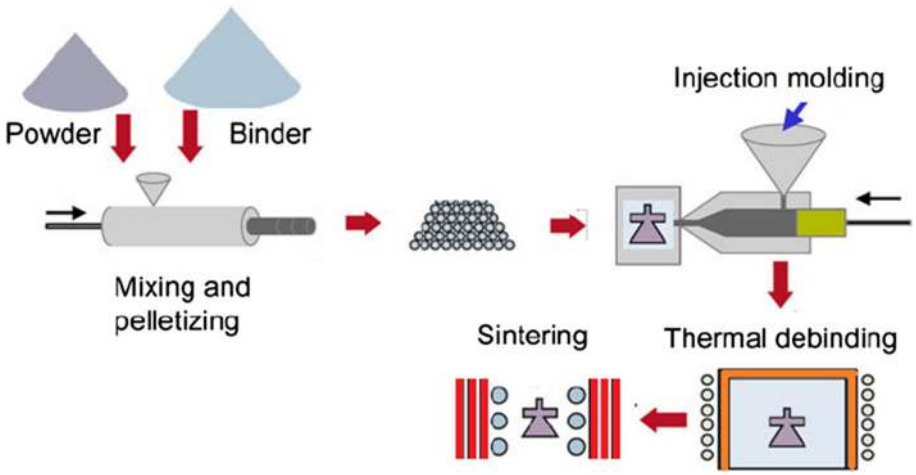

Fig. 1 Schematic diagram of whole PIM process, showing the basic steps from feedstock elaboration stage to sintered component

the separate particles are welded together and develop the final mechanical properties (see Fig. 1).

Recently, Tay et al. (2006) have succeeded in the manufacturing of micro-gears using the micro-powder injection molding process with 316L stainless steel powder possessing particle sizes of 2.4 μm and a multi-component wax-based binder system (Tay et al. 2006). The analysis revealed different grain structures at the tooth (≈35 μm) and hub of the micro-gear (≈5 μm). Significant grain growth was also observed at the tooth. Meng et al. (2011) conducted an experimental analysis on the replication of a micro-fluidic system by micro-powder injection molding using 316L stainless steel (Meng et al. 2011). Additionally, they also investigated the dimensional change and surface roughness of the micro-mixer. They obtained proper replication with appropriate shape retention lacking in visible defects by use of a powder injection molding process with a 316L stainless steel feedstock. The dimensional shrinkage of the micro-mixer occurred mainly in the sintering step, whilst the dimensional change was not noticeable in the debinding step. The surface topography of the silicon mold insert was properly replicated in the stainless steel micro-mixer.

Sintering is an essential PIM manufacturing stage used for making various parts from metal or ceramic powder mixtures. It can be defined as the thermal transformation of bulk materials into compact solids at temperatures below their melting point (Limberg et al. 2012; Mohsin et al. 2012; Nor et al. 2013; Choi et al. 2015). Sintering is a complex process influenced by many factors including temperature, sintering time, pressure and atmospheric composition, all of which determine the final properties of the sintered product (Chmielewski et al. 2010, 2012; Kaliński et al. 2012; Weglewski et al. 2012).

Because of the large shrinkage in sintering process, determination of the dimensional changes and distortions is necessary in industrial production to produce the components in near-net-shape and high quality. Besides the conventional trial and error method, numerical simulation of the sintering stage may be a fast and cost-effective alternative to solve this problem. Modeling of sintering process is still a challenging research task. Currently, there are different approaches to modeling sintering processes, ranging from continuum phenomenological models to micromechanical and atomistic ones (Tikare et al. 2010; Martin et al. 2014; Largiller et al. 2012; Pan 2003). The first analyses of sintering were based on the famous two sphere models that provided a simplified description of inter-particle neck growth and densification through miscellaneous diffusion mechanisms (Herring 1951; Kuczynski 1956; Coble 1958). Kuczynski (1949) studied mechanisms for neck growth and shrinkage during early sintering stages (particle bonding) using a two-sphere model (Kuczynski 1949). Coble (1961) developed a cylindrical pore model (Coble 1961). A spherical pore model for the later sintering stages was developed by MacKenzie and Shuttleworth (1949). The effect of particle size distributions on sintering has been studied by Wonisch et al. (2009). Then, a multiple mechanism calculations of one-dimensional shrinkage and the predictions of density including pressure-assisted sintering have been proposed (Blendell and Coble 1978; Bross and Exner 1979; Rosenzweig and Narkis 1981; Ramakrishnan et al. 1984; Takahashi et al. 1988; Sierra and Lee 1988; Belhadjhamida and German 1993; Kadushnikov et al. 1993). Schoenberg et al. (2006) compared analytical calculations and FE simulations to describe the sintering of a barium titanate cylindrical component composed of high- and low-density layers (Schoenberg et al. 2006). Nosewicz et al. (2013) presents an original viscoelastic model of powder sintering developed within the discrete element framework (Nosewicz et al. 2013). This model has been applied to the simulation of real process of sintering of Ni–Al powder. The model reproduces correctly the mechanism of free sintering and sintering under pressure. Finally, the sintering stage has been simulated using a continuum mechanics and finite element simulations of shape and size. They can be used to optimize and better

Table 1 Characteristics of the powders

Powders	Particle shape	d_{10} (μm)	d_{50} (μm)	d_{90} (μm)	Density (g/cm^3)	Tap density (g/cm^3)
316L stainless steel	Spherical	1.80	3.40	6.02	7.90	4.60
Copper	Irregular	3.73	6.34	10.81	9.80	4.63

understand this process to improve the quality of the sintered components. Mohsin et al. (2012) suggested a finite element analysis based on a thermo-kinetic model to describe the densification process of a MIM copper brown body during sintering (Nor et al. 2013). Song et al. (2006) investigated simulating the sintering process of 316L stainless steel powder components with a thermo-elasto-viscoplastic model (Song et al. 2006). Barriere et al. (2002, 2003) investigated the optimal process parameters by proposing adapted finite element modeling and simulation software for the MIM stage based on a biphasic model Barriere et al. (2002, 2003).

The purpose of this paper is to simulate the sintering of mono or bi-material of micro-components using a finite element method. First, we introduce constitutive equations that describe the behavior of both materials during sintering. These equations, which include both thermo-elastic and viscous terms, have been adjusted with data extracted from specific sintering experiments by the inverse method. Then, we plotted the results from the numerical simulation in terms of dimensional changes and relative densities.

2 Materials and experimental procedures

2.1 Powders and binder system

Fine spherically shaped 316L stainless steel powder ($D_{50} = 3.4$ μm) and irregularly shaped copper powder ($D_{50} = 6.3$ μm) were provided by Sandvik Osprey Company®. The powders had densities equal to 7.9 and 8.9 g cm^{-3}, respectively. Before mixing, the powders were dried in a vacuum oven at a temperature of 110 °C for 4 h to remove any moisture.

The binder components were polypropylene (PP), paraffin wax (PW) and stearic acid (SA). The composition of binder systems used with the stainless steel feedstock and copper feedstock is 40 vol% for PP, 55 vol% for PW and 5 vol% for SA. The characteristics of the binder systems and powders are shown in Tables 1 and 2.

2.2 Feedstock elaboration and characterization

By employing the proposed binder system, 316L stainless steel feedstock with a 60–66% solid loading fraction and copper feedstock with a solid loading fraction of 60% were used for the experiments. The mixing of the powders and

Table 2 Characteristics of the different binder components

Binders powders	Density (g/cm^3)	Melting temperature (°C)
Stearic acid (SA)	0.89	70
Paraffin wax (PW)	0.91	60
Polypropylene (PP)	0.90	160

binders was carried out using a twin screw mixer at 170 °C and 30 rpm for 30 min. The mixing torques were measured and plotted versus times for different stainless steel feedstocks in Fig. 2a. The observed torque peaks are due to the introduction of small amounts of feedstock into the mixture. It should be noted that the mixture with a solid loading of 62% had the lowest torque homogenization, reaching a value of approximately 2.4 N m. Therefore, the optimal load of stainless steel powder was identified to be 60%. Beyond a load of 64%, the feedstock did not demonstrate mixability. During the mixing tests, copper and stainless steel powders were found to be non-mixable for critical solid loads greater than or equal to 62 and 66%, respectively.

Figure 2b illustrates the mixing behavior of two different feedstocks with solid loadings of 62%, which are denoted as Copper and 316L stainless steel, respectively. The mixing torque of the feedstocks was identical in comparison to the constant torque level, it reaching a value of approximately 2.6 N m, which led to lower viscosity.

The rheological behavior of the feedstocks was measured using a capillary rheometer provided by Instruments Bohlin®. A series of experiments were performed in which the samples were extruded through a die with a 1 mm diameter and measuring 16 mm in length. Three temperatures were tested, including 170, 180 and 190 °C, beyond the melting temperature of the binder. Shear rates varying from 10^2 to 10^4 s^{-1} were applied using the die with the measurements reported above, giving a ratio (L/D) equal to 16. Figure 3a shows the apparent viscosity-shear rate curves of the extruded feedstock tested at different temperatures in the range of 170–190 °C. The feedstock viscosity decreases with shear rate and temperature, indicating pseudo-plastic flow behavior and increases with high powder volume ratios. Normally, the exhibition of pseudo-plastic flow by the feedstock during molding eases the mould filling process and minimizes jetting defects (German and Bose 1997; Hunt et al. 1988). Figure 3b shows the shear viscosity of the different feedstocks versus the shear rate, which were developed and mixed under the same

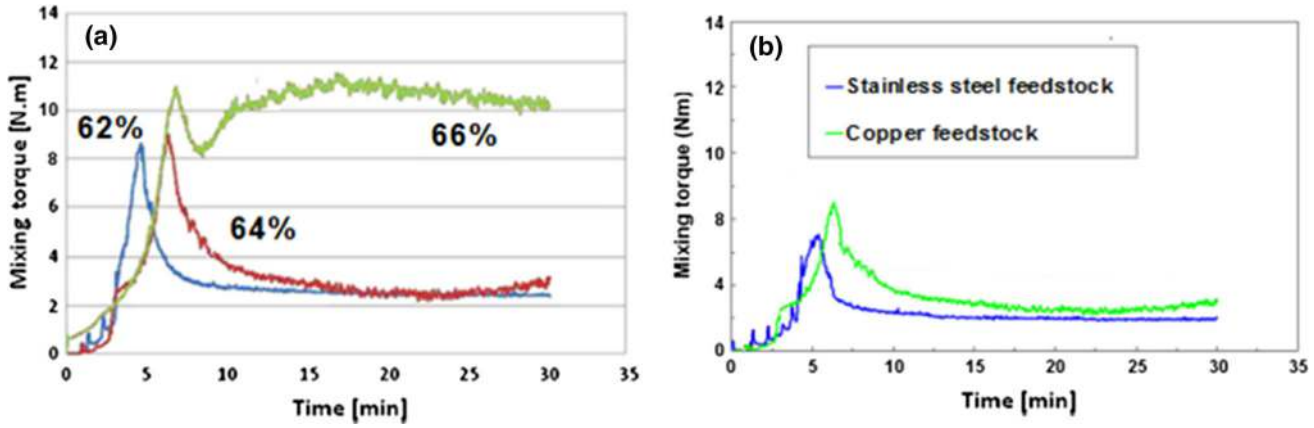

Fig. 2 Mixing torque vs. time for **a** different solid loadings corresponding to different stainless steel feedstock, **b** different feedstocks carried out with a mixing test (170 °C, 30 min and 30 rpm)

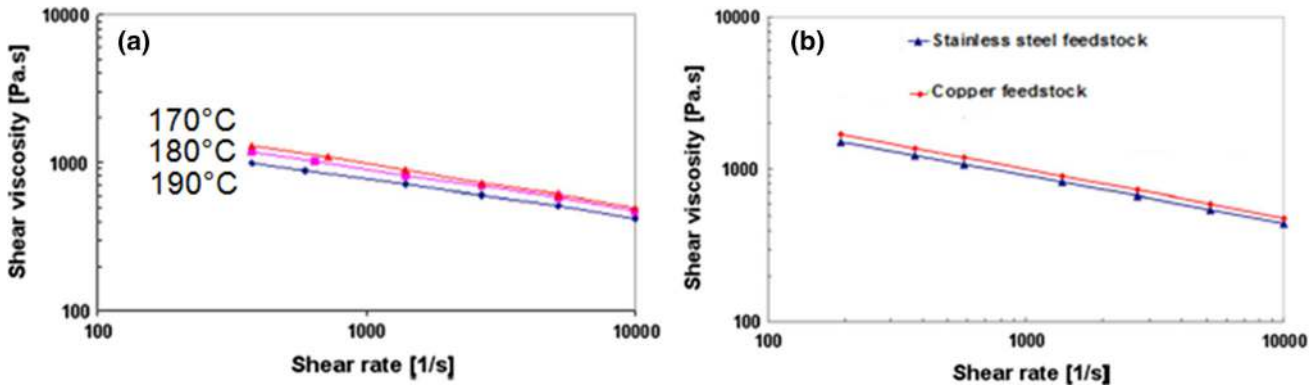

Fig. 3 **a** Viscosity of the 316L stainless steel feedstock with a solid loading of 60 %vol, tested at different temperatures, **b** viscosity of the different feedstocks analyzed at the same conditions (tested at 170 °C)

conditions and tested at 170 °C. The results indicate that the three feedstocks possess pseudo-plastic rheological behavior up to a shear rate of 10^4 s^{-1}. It was observed that the both feedstocks exhibited viscosities lower. This trend is the same as that observed for mixing torque.

3 Constitutive model for the sintering process

Compared with conventional trial and error methods, numerical simulations of sintering using finite element methods can be more effective by minimizing the effects of tooling and processing parameters (Yu et al. 2007). The model chosen for this investigation is a phenomenological model based on continuum mechanics and uses thermo-elasto-viscoplastic formulations (Song et al. 2006). The strain rate consists of three parts: the elastic strain rate $\dot{\varepsilon}_e$, the thermal strain rate $\dot{\varepsilon}_{th}$ and the viscoplastic strain rate $\dot{\varepsilon}_{vp}$. These are related by the following equation (Gasik and Zhang 2000):

$$\dot{\varepsilon} = \dot{\varepsilon}_e + \dot{\varepsilon}_{th} + \dot{\varepsilon}_{vp} \Rightarrow \dot{\varepsilon} = C_e\dot{\sigma} + \alpha\Delta\dot{T}I + \frac{dev(\sigma)}{2G} + \frac{\sigma_m - \sigma_s}{3K}I, \quad (1)$$

where C_e is the elastic compliance matrix, α is the thermal expansion coefficient, $\Delta\dot{T}$ is the incremental temperature rate, I is the second order identify tensor, α is experimentally determined using a dilatometer, $\sigma_m = tr(\sigma)/3$ is the trace of the stress tensor, I, G is the shear viscosity modulus, K is the bulk viscosity modulus, and σ_s is the sintering stress. The variables G, K and σ_s are material parameters that still need to be determined.

The elastic-viscous analogy is used to define the shear and bulk viscosity module for sintering materials (Song et al. 2010):

$$G_p = \frac{\eta_p}{2(1+\nu_p)}, \; K_p = \frac{\eta_p}{3(1-2\nu_p)} \quad (2)$$

where η_p and ν_p are the uni-axial viscosity and the viscous Poisson's ratio of a porous material, respectively. Song et al. derived the following relationship to define the

uniaxial viscosity η_p e through bending tests in a dilatometer (Bordia and Scherer 1988):

$$\eta_p^e = \frac{1}{\dot{\delta}}\left(\frac{5\rho_a g L_S^4}{32h^2} + \frac{PL_S^3}{4bh^3}\right) \tag{3}$$

where $\dot{\delta}$ is the deflection rate at the centre of the specimen, ρ_a is the apparent density, g is gravity, P is the external load, and L_s, b and h are the distance between the two supporting rods and thewidth and thickness of the specimen, respectively (Bordia and Scherer 1988).

Bordia and Scherer (1988) and Scherer (1979) relate a phenomenological expression to calculate Poisson's ratio of the sintered material as follows:

$$v_p \approx \frac{1}{2}\sqrt{\frac{\rho}{3-2\rho}},\ \rho = \frac{\rho_0}{(1+\lambda)^3}, \tag{4}$$

where ρ is the relative density ρ_0 and λ is the uni-axial shrinkage, which is defined as:

$$\lambda = \frac{L - L_0}{L_0} \tag{5}$$

where L_0 and L are the length of the specimens before and after sintering. The following equation is used to determine the sintering stress (Peterson and Agren 2004):

$$\sigma_S = B\rho^C \tag{6}$$

where B and C are material parameters identified from dilatometry experiments. Using these proposed constitutive equations, the related material parameters can be determined (German 2004; Kraft and Riedel 2004; Reiterer et al. 2004).

The identification algorithm is designed for the proper identification of material parameters B and C used in the sintering stress model to optimize the numerical simulations. The following equation was proposed to calculate the stress during the sintering stage (Peterson and Agren 2004):

$$\frac{1}{L}\frac{dL}{dt} = \alpha\Delta\dot{T} - \frac{1}{3K_p}\sigma_S. \tag{7}$$

The proper strategy consists of identifying parameters B and C in Matlab® that determine the numerical shrinkage curve according to Eq. (8). This curve is matched to that obtained from the free sintering tests. Therefore, the minimization algorithm is used to fit the simulations as best as possible to the experimental curves by adjusting the physical parameters (Peterson and Agren 2004):

$$\begin{cases} \min F(x) \\ F(x) = \sum_{i=1}^{n} |\lambda^m(T_i, x) - \lambda^e(T_i, x)|^2 \\ x = [B, C] \end{cases} \tag{8}$$

where λ_e is the experimental uni-axial shrinkage obtained from the dilatometry tests, λ_m is the numerical uni-axial shrinkage, F(x) is theme an residual squares of the tolerance, where i = 1,…, n indicates the different sintering temperatures and x is the set of material parameters that need to be identified (German 2004; Kraft and Riedel 2004; Reiterer et al. 2004).

4 Numerical simulations of the sintering process

Predicting uneven shrinkage of the sintering part is one of the important purposes of the sintering simulation. The initial geometries of the FE model were the mesh of the injection molded component obtained with ABAQUS®. Three different examples have been used in this work, composed of the micro-parts mono or bi-materials, and the supports are related through Fig. 4. The plate support and the micro-parts elements considered for the simulation are R3D4 and C3D8R elements, respectively. The plate support is assumed to be a rigid body during the simulations, and the coefficient of friction between the specimens and the support is set at 0.35. The "Pressure/Over-closure" contact was selected for the all components. In addition, the materials of micro-parts were also modeled using the constitutive equations defined in the previous paragraphs, also considering isotropic thermal and mechanical properties.

Several factors such as inhomogeneous green density, and friction between the supports and the parts were taking into account.

5 Numerical results and experimental validations

5.1 Micro-gears

The radial shrinkage in the micro-gears at different sintering temperature is related in Fig. 5. The results of all these simulations show isotropic shrinkage behavior; this is due to the axisymmetric of the spur gear geometry. The maximum of the isotropic shrinkage have been observed on the teeth of the sprocket and obtained for a thermal kinetics corresponding to 10 °C/min. The shrinkage of the sample sintered at 1360 °C increases to 14.45% from its original. The maximum shrinkage occurs at the tooth surfaces and illustrates the distortion often induced in the final sintered component.

The variation of the relative density versus the sintering temperature for the micro-gears is presented in Fig. 5 where it can be seen that the relative density of the specimens increases with the increment of the sintering temperature. It can be also observed that the sintering process makes the final density of the sintered bodies almost uniform. Homogeneous green relative densities equal 0.6, 0.62 and 0.64 have been used in simulation corresponding to the, feedstock loaded at 60, 62 and 64%, respectively. It can be seen that the relative density of micro-gears

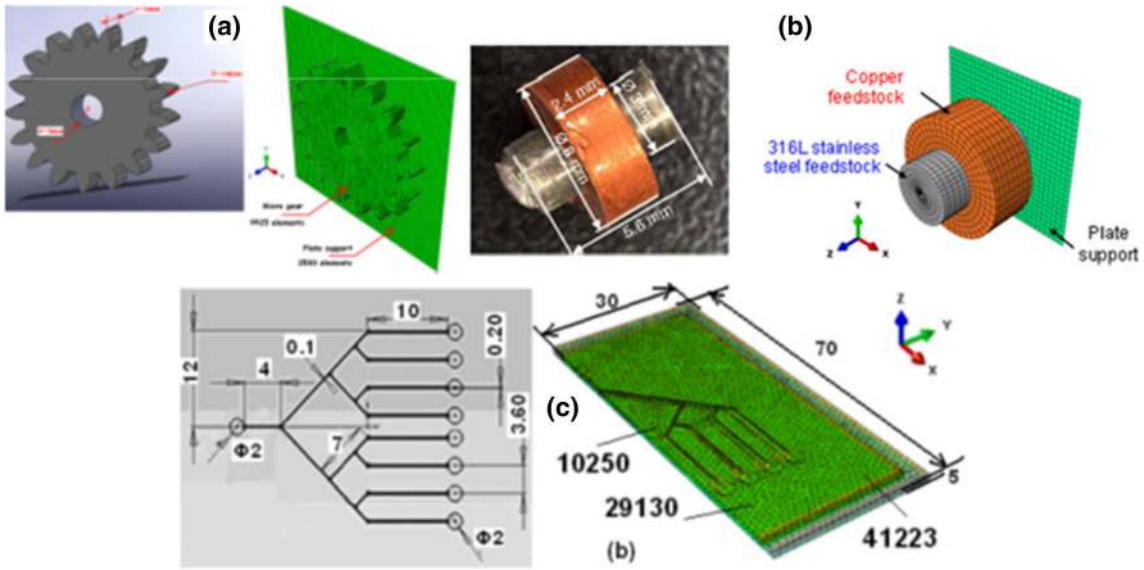

Fig. 4 CAD model and FE meshes of **a** the micro-gears, **b** micro-bi-material component, **c** micro-fluidic specimens and the plate support prior to the sintering stages. Dimensions of samples as sintered condition (units are in mm)

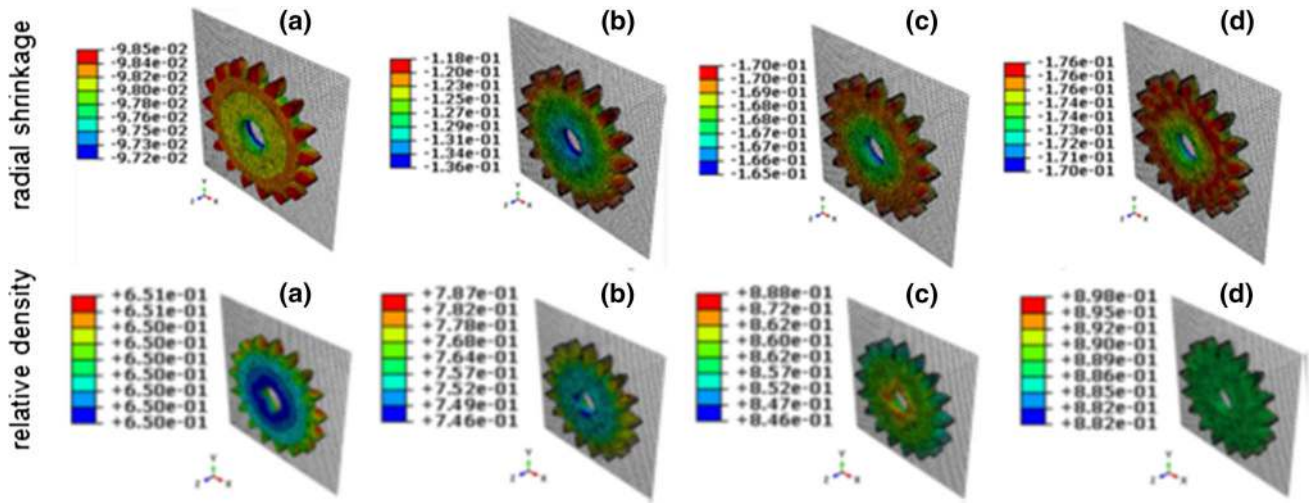

Fig. 5 Numerical radial shrinkage and final distribution of the relative density in micro-gears versus sintering temperature: **a** 1050 °C, **b** 1150 °C, **c** 1250 °C and **d** 1360 °C (heating rate, 10 °C/min; solid loading of 60%, unit %)

increases with increasing of the sintering temperature; the relative density is up 95% when the sintering temperature is 1360 °C. This indicated that the increase of the sintering temperature is in favor of the densification of stainless steel parts.

The homogeneity of the green parts is induced by the previous processes before the sintering, such as the mixture of powders and binders, pressing or injection molding (German 2004; Kraft and Riedel 2004; Reiterer et al. 2004). In this case, the simulation is carried out with a green part assumed homogeneous after injection stage. Its relative density varied from 0.6 to 0.64. One was also found that when solid loading is increased, shrinkage was decreased. The micro-gear loading with 64% solid was optimum for 316L stainless steel feedstock, which showed the best physical properties. This agrees with previous results, which suggest that optimum solid loading of stainless steel was 60% (see Fig. 6).

Besides of shrinkages, the relative densities have been simulated as well for these micro-gears injected with solid loading of 60, 62 and 64%, respectively. The relative density distributions of the sintered micro-gears have been illustrated in Fig. 6. As it is shown in the figures, the relative densities are generally homogeneous for most of the simulations, in which the variations have been well controlled within 4%. However, some little better results have been obtained in the first and

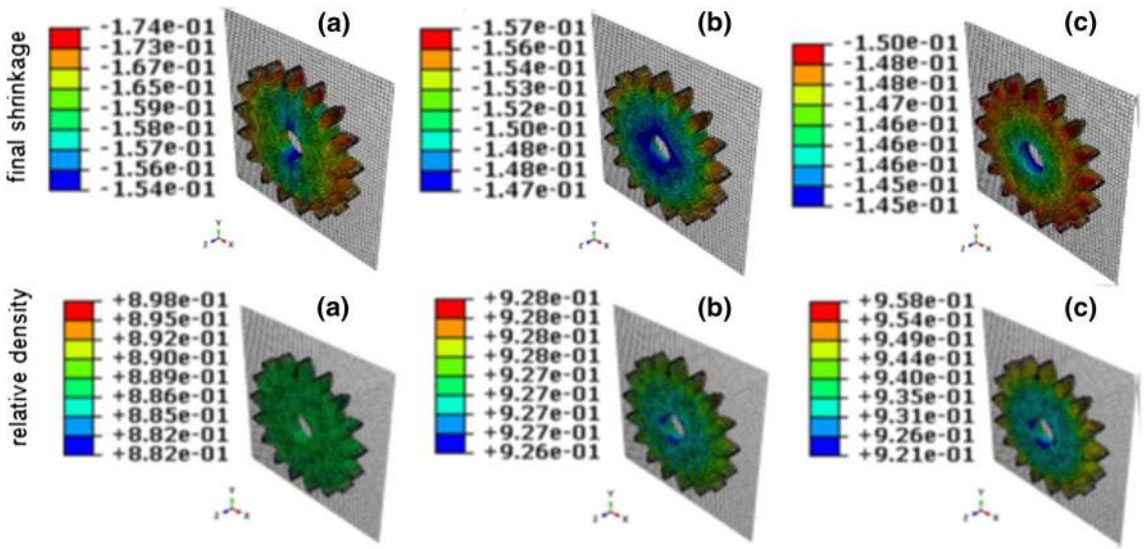

Fig. 6 Numerical final shrinkage and final distribution of the relative density in the sintered micro-gears versus solid loading: **a** 60%, **b** 62% and **c** 64% (sintering temperature, 1360 °C; heating rate, 10 °C/min, unit %)

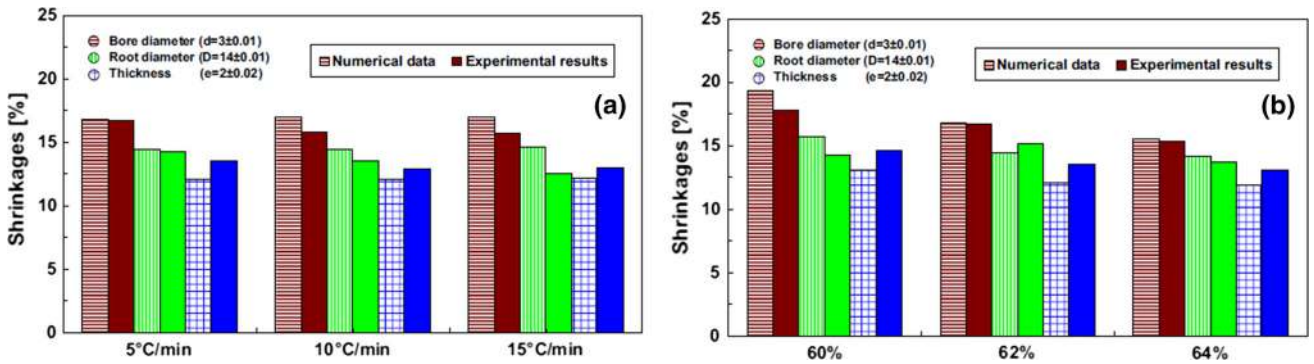

Fig. 7 Comparison between the experimental and numerical shrinkage for the micro-gear component sintered at 1360 °C using a different heating rates (solid loadings, 62%) and **b** different solid loadings (heating rate, 5 °C/min)

second ones (solid loading, 60 and 62%; heating rate, 10 °C/min). It has been shown also that the components loaded higher are particularly more sensitive to the rapid heating rate.

The mean shrinkage in the main directions is illustrated in Fig. 7. The results show that the feedstock loaded at 60%, with a sintering cycle utilizing an heating rate of 5 °C/min results in the maximum shrinkage. Very high shrinkage in thickness direction was also observed for the micro-component injected with stainless steel feedstock loaded at 60%. The numerically determined curves compare well with the experimental ones for the three different heating rates. Additionally, these results were confirmed by the choice of the sintering stress model and the identification method in our work.

In addition, the relative densities of the sintered micro-gears were measured by the water displacement method (Archimede method) for the feedstocks loaded from 60 to 64%, as reported in Fig. 8. The relative density was calculated as the ratio of the measured density to the theoretical density. All specimens subjected to density measurements were ultrasonically cleaned in an alcohol bath for 10 min and rinsed in distilled water for an additional 10 min to remove any contaminants. The specimens were then dried with adsorbent paper towels. The average random and systematic errors in the density measurements were quantified as 3%. The sintered micro-gears using stainless steel feedstocks reached relative maximum densities between 92 and 97%. The relative densities were in perfect agreement with the experimental densities, especially for the sintering cycles with relatively low heating rates.

5.2 Bi-material components

The final shrinkage in the micro-bi-material components after the numerical simulations for a powder volume

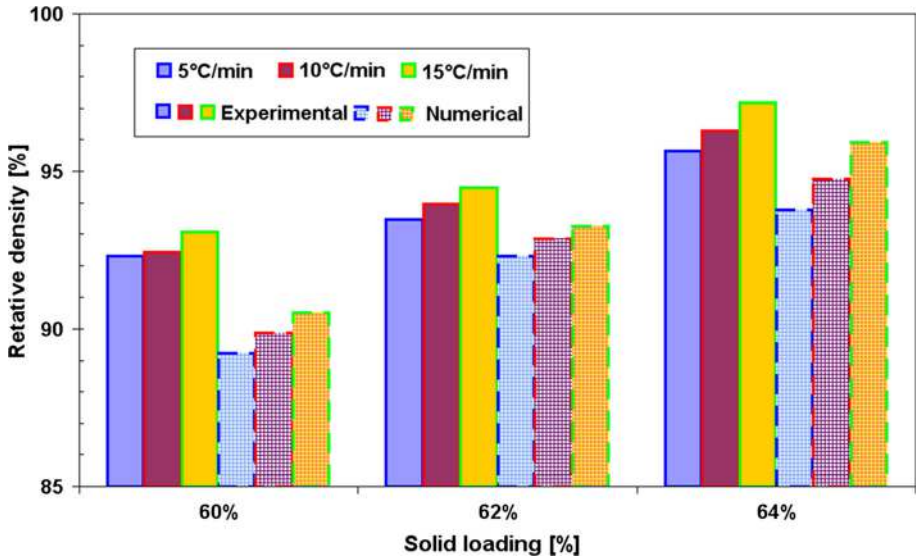

Fig. 8 Density variation of the sintered micro-gears fabricated using 316L stainless steel feedstock

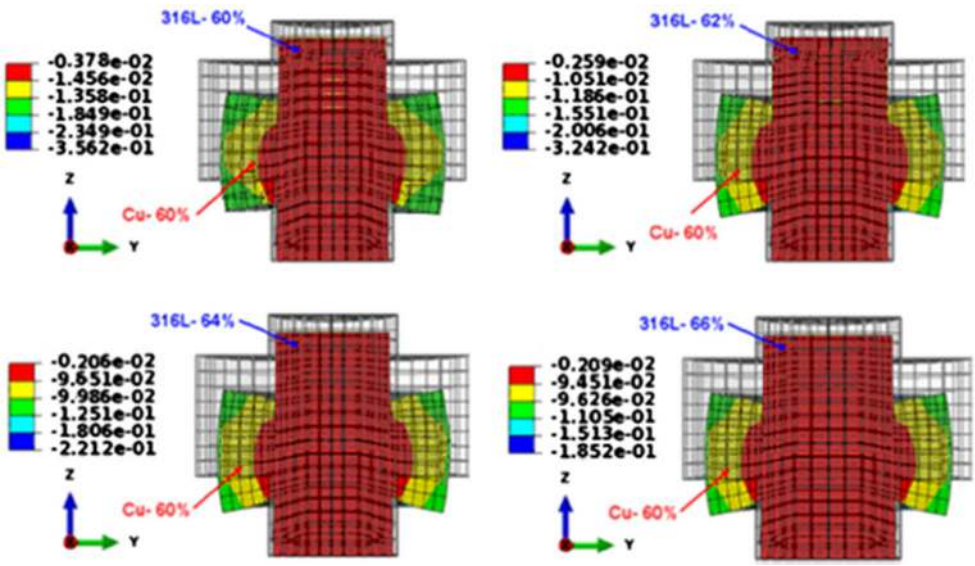

Fig. 9 Numerical final shrinkage of the sintered micro-bi-material component (316L stainless steel feedstock at solid loadings of 60, 62, 64, 66% and copper feedstock at a solid loading of 60%) after sintering at 1000 °C (heating rate: 15 °C/min, hold time: 12 min)

loading from 60 to 66% for the 316L stainless steel feedstock and a powder volume loading of 60% for the copper feedstock is illustrated in Fig. 9. A distortion exists on the contact surface between the 316L stainless steel and copper. This is likely the result from unbalanced sintering shrinkage kinetics between the two materials. Careful control over the powder volume loading is important to control the shrinkage between the materials. Indeed, the outer part exhibits more shrinkage to ensure constant contact between the two materials.

Besides of shrinkages, the relative densities have been simulated as well for these micro-bi-material components injected with different solid loading. The relative density distributions of the sintered micro-parts have been illustrated in Fig. 10. As it is shown in the figures, the relative densities are generally homogeneous for most of the simulations, in which the variations have been well controlled within 6%. It can be also seen that the relative density of micro-parts increases steadily with increasing of heating rates. This indicated that the increase of the heating rates is in favor of the densification of micro-parts. The relative density of the specimens can be also increased with the increment of the sintering temperature and solid loading.

During our investigations, bi-material micro-injection molding equipment was used to inject both 316L stainless steel and copper feedstock into die mould cavities. The resulting component from this bi-material injection stage is shown in Fig. 11a. The central cylinder (Ø3 mm × 5.6 mm) is injected with the 316L stainless steel feedstock, whereas the ring (Ø6 mm × 2.4 mm) around the central cylinder corresponds to the copper feedstock. In addition,

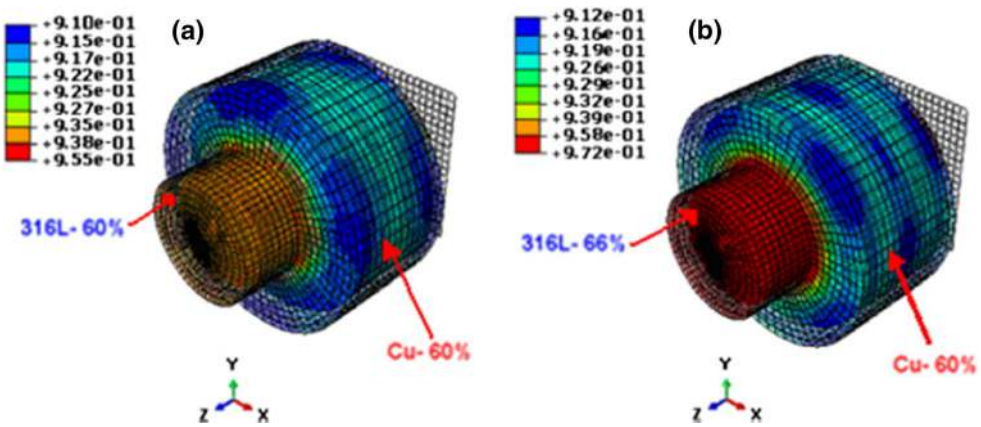

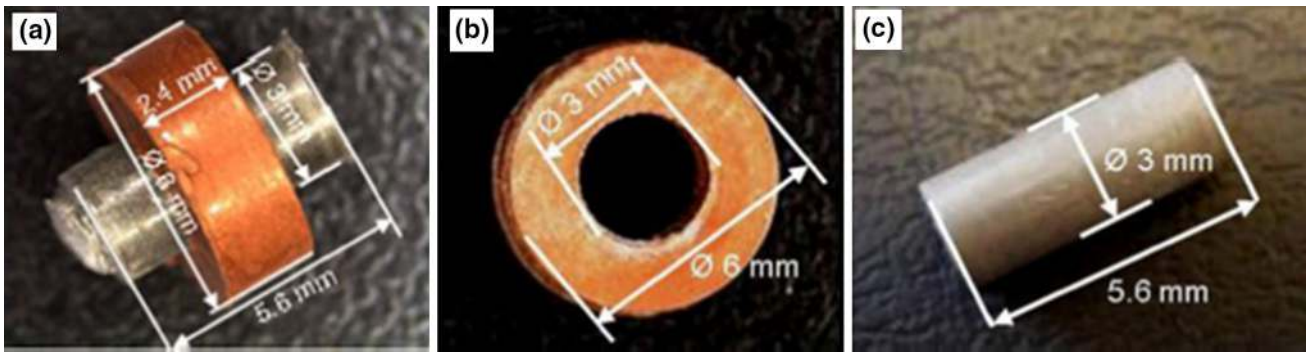

Fig. 10 Final numerical relative density of the sintered micro-bi-material component after sintering at 1000 °C and heating rate equal to: **a** 10 °C/min and **b** 15 °C/min (hold time: 120 min)

Fig. 11 **a** Micro-bi-material component injected with the 316L stainless steel feedstock (solid loading of 60%) and copper feedstock (solid loading of 60%), **b** ring component injected with the copper feedstock and **c** cylinder component injected with the 316L stainless steel feedstock

the central cylinder and the ring can be injected separately, as shown in Fig. 11b.

The main injection parameters are the same for both the simultaneous and separate injection operations, including an injection temperature of 220 °C, an injection pressure of 40bars, and injected volumes of 45 mm^3 for the 316L stainless steel feedstock and 60 mm^3 for the copper feedstock. Figure 12 shows the correctly debinded and sintered components. There are no obvious defects or cracks at the interface of the different feedstocks, even along the interface zone.

The dimensional analyses were carried out on the three sintered specimens injected with different feedstock loaded from 60 to 64%. The same debinding kinetics rate was used for both feedstocks. The injection, debinding and sintering stages of ring micro parts were performed after sintering the cylindrical micro-parts. The mean shrinkage in the main directions is illustrated in Fig. 13. The results show that the feedstock loaded at 60%, with a sintering cycle utilizing a heating rate of 5 °C/min results in the maximum shrinkage. Very high shrinkage in thickness direction was also observed for the ring component injected with copper feedstock loaded at 60%. This same phenomenon has been encountered by other researchers, such as Loh and German (1996). The main parameters affecting the final part size have already been studied and include the metal powder morphology, binder ingredients and proportions, mixing conditions, mould design, molding parameters, rheological behavior of the molding materials, debinding, sintering, equipment and even environmental conditions. Among these often integrally related factors, the most sensitive are the powder volume loading and the mould design (Loh and German 1996). Additionally, these results were confirmed by the choice of the sintering stress model and the identification method in our work.

In addition, the relative densities of the sintered micro-components (cylindrical, ring and bi-material components) were measured by the water displacement method (Archimede method) for the feedstocks loaded from 60 to 64%, as reported in Table 3. The relative density was calculated as the ratio of the measured density to the theoretical density. All specimens subjected to density measurements were ultrasonically cleaned in an alcohol bath for 10 min and rinsed in distilled water for an additional 10 min to remove any contaminants. The specimens were then dried with adsorbent paper towels. The average random and systematic errors in the density measurements were quantified as 3%. The sintered

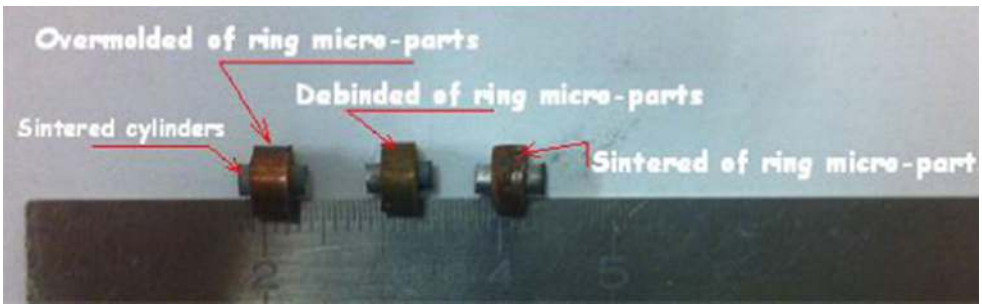

Fig. 12 Photographs of the bi-material micro-specimens obtained after injection, debinding and sintering using copper feedstock loaded at 60% and stainless steel feedstock loaded at 60%

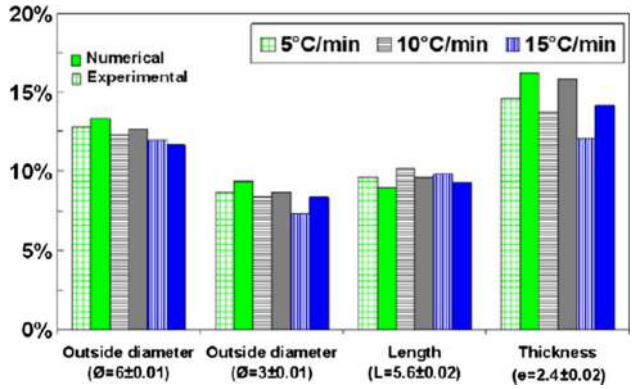

Fig. 13 Comparison of the experimental and numerical shrinkage for the bi-material component after sintering at different heating rates (copper and stainless steel feedstocks, sintered temperature: 1000 °C, solid loading: 60%, units: mm)

micro-parts using copper or stainless steel feedstocks reached relative maximum densities of 92 and 97%, respectively.

5.3 Micro-fluidic die mold cavity

The simulation of the micro-fluidic replicas as was also carried out with the Abaqus® finite element solver based on the above models and identified parameters. In the powder injection molding process, the segregation occurs between the powders and the binders due to their different inertia. It induces the inhomogeneous density distributions in the green parts. This initial in-homogeneity affects the final dimensions and mechanical properties of the sintered components. This one has been taken into account in this case.

The initial and final distribution of relative density after injection and sintering stages, respectively obtained by simulation, is shown in Fig. 14. It can be observed that the final density distribution is still almost uniform, despite that the green parts were initially inhomogeneous one. Figure 14a displays the relative density distribution contour after powder injection molding process, with its lowest value of 61.20% in the central area and highest density of 62.4% to the outside of the micro-fluidic component. The relative density gap was broadened by about 1% during injection molding, which was narrowed after sintering. It is mainly due to the considerable compression effects and feedstock flow in die mould cavities as well as the non-homogeneous loading conditions in terms of the complicated structure. It indicates also that sintering assists in balancing the density distribution and narrowing the in-homogeneity.

The influence of the heating rates on the density of the sintered parts is shown in Fig. 15. The sintering process makes the sintered components with a nearly uniform final density distribution in spite of the inhomogeneous green density distribution due to the segregation occurring in the injection step. After sintering stage, the relative densities are generally homogeneous for most of the simulations, in which the variations have been well controlled within 2%. One was found that heating rate has a significant effect on

Table 3 Density of the sintered micro-parts fabricated from the copper and stainless steel feedstocks

	Heating rate (°C/min)	Solid loading	Density (g/cm^3)			Relative density		
			60%	62%	64%	60%	62%	64%
Cylindrical components	5		7.20	7.21	7.26	92.30	92.43	93.07
	10		7.29	7.33	7.37	93.46	93.97	94.48
	15		7.46	7.51	7.58	95.64	96.28	97.18
Ring components	5		8.15	–	–	90.95	–	–
	10		8.23	–	–	91.85	–	–
	15		8.31	–	–	92.74	–	–

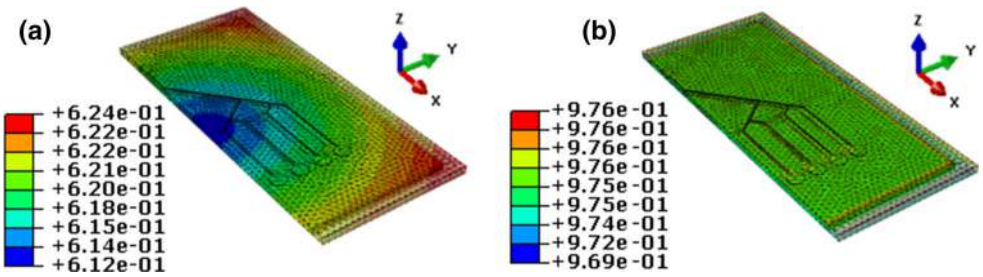

Fig. 14 Final distribution of the relative density in micro-fluidic specimens of 316L stainless steel powders, obtained after **a** injection molding process and **b** sintering stage at 1360 °C (solid loading: 60%, heating rate: 15 °C/min, hold time: 120 min)

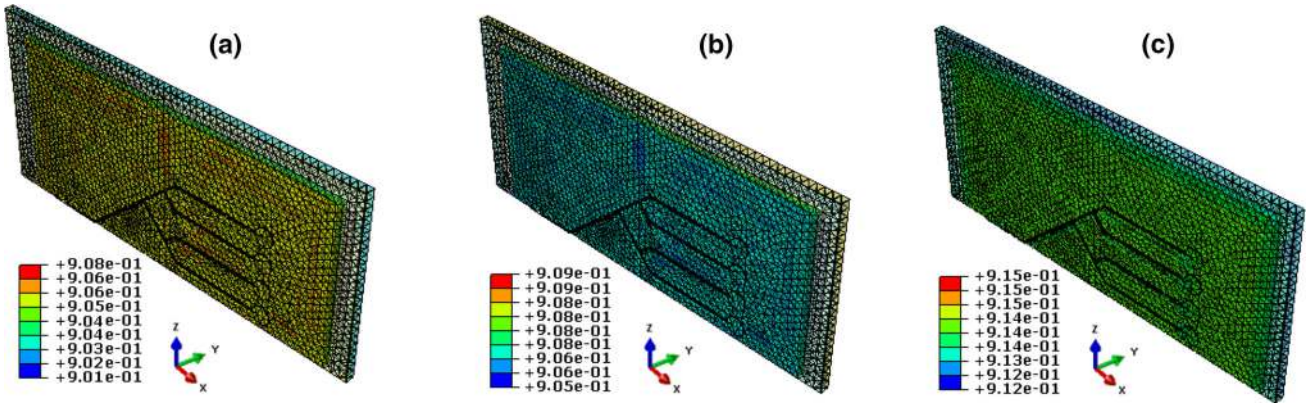

Fig. 15 Final numerical relative density of the sintered micro-fluidic components after sintering at 1250 °C and heating rate equal to: **a** 5 °C/min, **b** 10 °C/min and **c** 15 °C/min (solid loading: 60%, hold time: 120 min)

the sintered density only at 1250 °C, increasing the average sintered density from 7.11 to 7.27 g/cm^3. It can be observed that the final density distribution is still almost uniform, more homogeneous when the heating rate equal to 15 °C/min. In addition, numerical data clearly indicated that the sintering temperature has a significant effect on the sintered density. In fact, increasing the sintering temperature from 1150 to 1360 °C resulted in the average density increasing from 6.16 to 7.66 g/cm^3. In practice this can be explained in fact by a more intensive atomic diffusion that can be caused by the higher sintering temperatures, resulting in faster sintering and higher resulting densities. Generally, all the sintering variables have a significant effect on the sintered density. The numerical data showed that the sintering temperature has the highest influence on the sintered density (64%), followed by the heating rate (8%), the solid loading (4%) and the two-factor and three-factor interactions. Other sintering variables, not taken into account in our simulations, have been also a significant effect on the sintered density such as the sintering atmosphere and the sintering time.

It is obvious that rapid sintering is favorable to densification, but fast sintering can induce the crack in sintered body due to the high thermal or stress gradients (German and Lathrop 1978). In addition, the final shrinkage decreases with increasing solid loading (see Fig. 16). It clearly seen that the shrinkage value was stable and homogeneous, this is mainly due to the symmetrical geometry. In addition, the shrinkage values increases with increasing heating rate, with a shrinkage value more stable and homogeneous observed at 15 °C/min.

The relative density of the micro-fluidic specimens obtained from the numerical simulations is compared with the experimental ones, as shown in Fig. 17. The relative densities were in perfect agreement with the experimental densities, especially for the sintering cycles with relatively low heating rates. The values of relative density are lower than the experimental ones with maximum discrepancy are less than 3%. The results from simulation are almost smaller than the ones from experiment; this is due to the fact that the identification tests in the vertical dilatometer have been carried out in an argon atmosphere instead of vacuum to prevent them from getting oxidized. As it is known, in some worse situations, the pores will be coarsen due to the inner expansion of the gas in the pores when the sintering is processed at high temperature (German 1990; Henrich et al. 2007), the consequence is that the slow down and the reduction effect for densification, but there no gas trapped when the sintering stage is carried out in vacuum atmosphere, that's why the experimental results are always higher than the ones simulated by using the identified parameters from the vertical tests.

A comparison between the experimental and the simulation results of the shrinkage in three directions (length, width and height) is shown in Fig. 18. During the sintering stage, the simulated dimensions were in good accordance

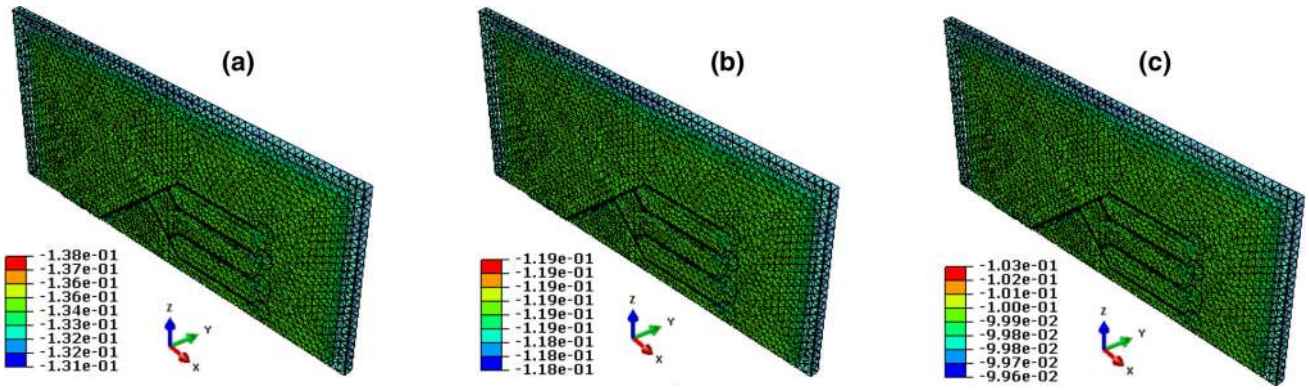

Fig. 16 Numerical final shrinkage of the sintered micro-fluidic components after sintering at 1360 °C using different solid loading **a** 60%, **b** 62% and **c** 64% (heating rate: 15 °C/min, hold time: 120 min)

Fig. 17 Comparison between the experimental and simulated results of the relative density

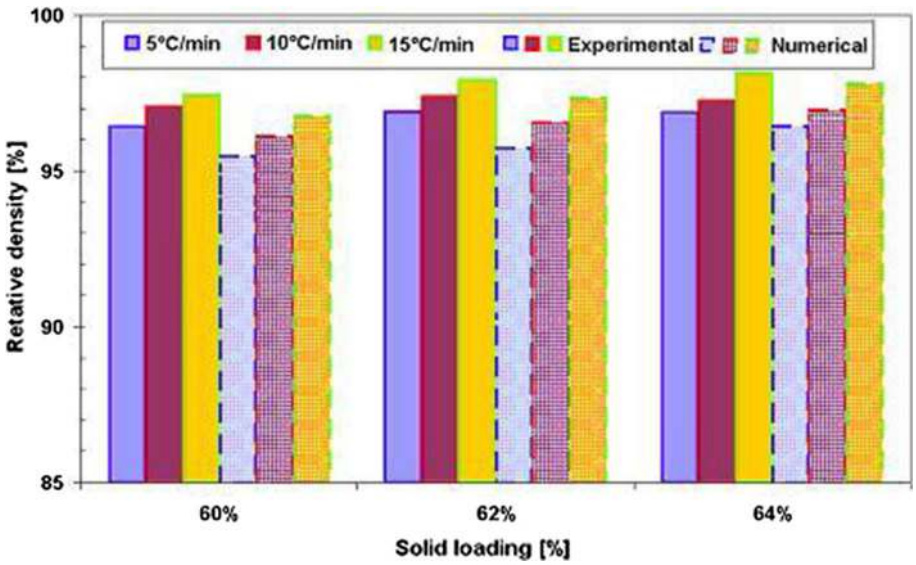

with the experimental ones, with a relative error of less than 3% in the both directions. The experimental shrinkages in all three dimensions were larger than the simulated ones. In addition, both the simulated and experimental shrinkages in the height direction were higher than those in other two directions, mainly due to the gravity along the height direction. During the sintering process, the relative error between the simulated and the experimental results in the height direction were found to be a greater than 5%. This result was mainly due to the structural anisotropy of parts processed. This same phenomenon has been encountered by other researchers, such as Loh and German (1996).

In the future, it is expected to use the proper experimental methods, such as coordinate measuring machine, to measure the uneven shrinkages of the sintered parts in complex shape. These experimental results can be employed to verify the simulation results.

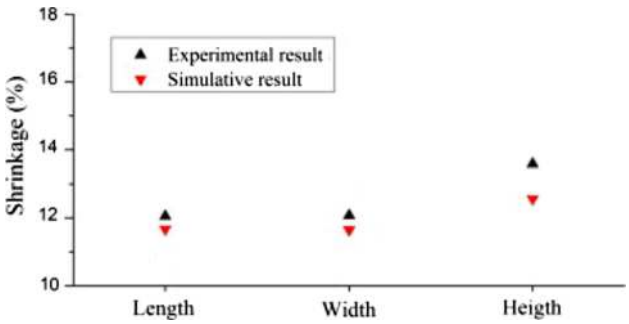

Fig. 18 Comparison between the experimental and simulated results of shrinkage in three directions

6 Conclusions

The paper summarizes experimental and numerical results carried out on micro-PIM process. The findings can be summarized as follows:

1. A phenomenological model describing the thermal/mechanical behavior during the sintering process was proposed, and the involved material parameters were identified from the results of specific experiments. The model makes no assumptions about the shapes of the particles and their relative sizes. However, the model correctly reproduces the free-sintering mechanism.
2. The modeling of sintering stage by using FE simulation has been also proven that an efficient method to predict shrinkage of MIM components. The FE model results were compared with experimental results and that showed a good agreement. The micro-components exhibit inhomogeneous shrinkage after sintering ranging from 14 to 18%, depending on the solid loading and sintering temperature and heating kinetics. We have been also demonstrate that the mechanical properties of these micro-parts can be predicted before sintering with high accuracy using FE methods.

In order to improve the accuracy of the simulation results, the powder in-homogeneity in the molded parts has to be accounted as well as friction coefficient between the parts and sintering supports that should be properly defined. Further extensions of the viscoelastic model, modeling of the individual powder particles and pores and the formulation of the micro-structural changes are presently under development.

Compliance with ethical standards

Funding This study was not funded by any Company.

Conflict of interest All the authors have not received research grants, a speaker honorarium from any Company and own not stock in any Company. All the authors are not a member of any committee. OR if no conflict exists: The authors declare that they have no conflict of interest.

References

Barriere T, Gelin J-C, Liu B (2002) Improving mould design and injection parameters in metal injection moulding by accurate 3D finite element simulation. J Mater Process Technol 125–126:518–524

Barriere T, Liu B, Gelin J-C (2003) Determination of the optimal process parameters in metal injection molding from experiments and numerical modeling. J Mater Process Technol 143–144:636–644

Belhadjhamida A, German RM (1993) A model calculation of the shrinkage dependence on rearrangement during liquid phase sintering. Adv Powder Metall Part Mater Metal Powder Ind Fed Princeton NJ 3:85–98

Blendell JE, Coble RL (1978) Test by numerical simulation of applicability of steady state diffusion models in final stage sintering. Powder Metall Int 10:65–68

Bleyan D, Hausnerova B, Svoboda P (2015) The development of powder injection moulding binders: a quantification of individual components' interactions. Powder Technol 286:84–89

Bordia RK, Scherer GW (1988) On constrained sintering. I. Constitutive model for a sintering body. Acta Mater 36:2393–2397

Bricout J, Matheron P, Ablitzer C, Gelin J-C, Brothier M, Barriere T (2015) Evaluation of the feasibility of the powder injection moulding process for the fabrication of nuclear fuel and comparison of several formulations. Powder Technol 279:49–60

Bross P, Exner HE (1979) Computer simulation of sintering processes. Acta Metall 27:1013–1020

Chmielewski M, Kaliński D, Pietrzak K, Włosiński W (2010) Relationship between mixing conditions and properties of sintered 20AlN/80Cu compositematerials. Arch Metall Mater 55:579–585

Chmielewski M, Dutkiewicz J, Kaliński D, Litynska-Dobrzynska L, Pietrzak K, Strojny-Nedza A (2012) Microstructure and properties of hot-pressed molybdenum-alumina composites. Arch Metall Mater 57:687–693

Choi J-P, Lee G-Y, Song J-I, Lee W-S, Lee J-S (2015) Sintering behavior of 316L stainless steel micro-nanopowder compact fabricated by powder injection molding. Powder Technol 279:196–202

Coble RL (1958) Initial sintering of alumina and hematite. J Am Ceram Soc 41:55–62

Coble RL (1961) Sintering of crystalline solids. I. Intermediate and final state diffusion models. J Appl Phys 32:787–792

Contreras JM, Jiménez-Morales A, Torralba JM (2009) Fabrication of bronze components by metal injection moulding using powders with different particle characteristics. J Mater Process Technol 209:5618–5625

Fu G, Loh NH, Tor SB, Murakoshi Y, Maeda R (2004) Replication of metal microstructures by micro powder injection moulding. Mater Des 25:729–733

Gasik M, Zhang B (2000) A constitutive model and FE simulation for the sintering process of powder compacts. Comput Mater Sci 18:93–101

German RM (1990) Powder injection molding. MPIF, Princeton

German RM (1997) The production of stainless steels by injection molding water atomized pre-alloy powders. J Inject Mold Technol 1:171–180

German RM (2004) Green body homogeneity effects on sintered tolerances. Powder Metal 47:157–160

German RM, Bose A (1997) Injection molding of metals and ceramics. Metal Powder Industries Federation, Princeton, pp 99–132

German RM, Lathrop JF (1978) Simulation of spherical powder sintering by surface diffusion. J Mater Sci 13:921–929

Han JS, Gal CW, Kim JH, Park SJ (2016) Fabrication of high-aspect-ratio micro piezoelectric array by powder injection molding. Ceram Int 42:9475–9481

He H, Li Y, Lou J, Li D, Lui C (2016) Prediction of density variation in powder injection moulding-filling process by using granular modelling with interstitial power-law fluid. Powder Technol 291:52–59

Heaney DF, Gurosik JD, Binetj C (2005) Isotropic forming of porous structures via metal injection moulding. J Mater Sci 40:973–981

Henrich B, Wonisch A, Kraft T, Moseler M, Riedel H (2007) Simulations of the influence of rearrangement during sintering. Acta Mater 55:753–762

Herring C (1951) Surface tension as a motivation for sintering. In: Kingston WE (ed) The physics of powder metallurgy. McGraw-Hill, New York, pp 143–179

Hunt KN, Evans JRG, Woodthorpe J (1988) The influence of mixing route on the properties of ceramics injection molding blends. Br Ceram Trans 87:17–21

Kadushnikov RM, Skorokhod VV, Lykova OB (1993) Computer simulation of the evolution of the microstructure of two-phase

polydispersed materials during sintering. Powder Metall Metal Ceram 32:292–298
Kaliński D, Chmielewski M, Pietrzak K (2012) An influence of mechanical mixing and hot pressing on properties of NiAl/Al2O3 composite. Arch Metall Mater 57:694–702
Kraft T, Riedel H (2004) Numerical simulation of solid state sintering: model and application. J Eur Ceram Soc 24:345–361
Kuczynski GC (1949) Self diffusion in sintering of metallic particles. Metal Trans 185:169–178
Kuczynski GC (1956) The mechanics of densification during sintering ofmetallic particles. Acta Metall 4:58–61
Largiller G, Dong L, Bouvard D, Carry CP, Gabriel A (2012) Deformation and cracking during sintering of bimaterial components processed from ceramic and metal powder mixes. Part II: numerical simulation. Mech Mater 53:132–141
Lebib A, Chen Y, Bourneix J, Carcenac F, Cambril E, Couraud L, Launois H (1999) Nanoimprint lithography for a large area pattern replication. Microelectron Eng 46:319–322
Limberg W, Ebel T, Pyczak F, Oehring M, Schimansky FP (2012) Influence of the sintering atmosphere on the tensile properties of MIM-processed Ti 45Al 5Nb 0.2B 0.2C. Mater Sci Eng A 552:323–329
Loh NH, German RM (1996) Statistical analysis of shrinkage variation for powder injection molding. J Mater Process Technol 59:278–284
Martin S, Guessasma M, Léchelle J, Fortin J, Saleh K, Adenot F (2014) Simulation of sintering using a non smooth discrete element method. application to the study of rearrangement. Comput Mater Sci 84:31–39
McKenzie JK, Shuttleworth R (1949) A phenomenological theory of sintering. Proc Phys Soc B 62:833–852
Meng J, Loh NH, Fu G, Tay BY, Tor SB (2011) Micro powder injection moulding of alumina micro-channel part. J Eur Ceram Soc 31:1049–1056
Mohsin UI, Lager D, Hohenauer W, Gierl C, Danninger H (2012) Finite element sintering analysis of metal injection molded copper brown body using thermo-physical data and kinetics. Comput Mater Sci 53:6–11
Mukund BN, Hausnerova B, Shivashankar TS (2015) Development of 17-4PH stainless steel bimodal powder injection molding feedstock with the help of interparticle spacing/lubricating liquid concept. Powder Technol 283:24–31
Nor NHM, Muhamad N, Ihsan AKAM, Jamaludin KR (2013) Sintering parameter optimization of Ti-6Al-4 V metal injection molding for highest strength using palm stearin binder. Proc Eng 68:359–364
Nosewicz S, Rojek J, Pietrzak K, Chmielewski M (2013) Viscoelastic discrete element model of powder sintering. Powder Technol 246:157–168
Packianather M, Chan F, Griffiths C, Dimov S, Pham DT (2013) Optimisation of micro injection moulding process through design of experiments. Procedia CIRP 12:300–305
Packianather M, Griffiths C, Kadir W (2015) Micro injection moulding process parameter tuning. Procedia CIRP 33:400–405
Pan J (2003) Modelling sintering at different length scales. Int Mater Rev 2(17):69–85
Peterson A, Agren J (2004) Constitutive behavior of WC-Co materials with different grain size sintered under load. Acta Mater 52:1847–1858
Petzoldt F (2008) Micro powder injectionmoulding-challenges and opportunities. Powder Injec Mould Int 2:37–42
Ramakrishnan N, Bhat TB, Arunachalam VS (1984) An analysis of pressure sintering by computer simulation. Acta Metall 32:357–370
Raza MR, Sulong AB, Muhamad N, Akhtar MN, Rajabi J (2015) Effects of binder system and processing parameters on formability of porous Ti/HA composite through powder injection molding. Mater Des 87:386–392
Reiterer M, Kraft T, Janosovits U, Riedel H (2004) Finite element simulation of cold isostatic pressing and sintering of SiC components. Ceram Int 30:177–183
Rosenzweig N, Narkis M (1981) Dimensional variations of two spherical polymeric particles during sintering. Polym Sci Eng 21:582–585
Ruprecht R, Gietzelt T, Müller K, Piotter V, Haußelt J (2002) Injection molding of microstructured components from plastics, metals and ceramics. Microsyst Technol 8:351–358
Scherer GW (1979) Sintering inhomogeneous glasses: application to optical waveguides. J Non-Cryst Solids 34:239–256
Schoenberg SE, Green DJ, Segall AE, Messing GL, Grader AS, Halleck PM (2006) Stresses and distorsion due to green density gradients during densification. J Am Ceram Soc 89:3027–3033
Sierra CM, Lee D (1988) Modeling of shrinkage during sintering of injection molded powder metal compacts. Powder Metall Int 20:28–33
Song J, Gelin J-C, Barrière T (2006) Experiments and numerical modelling of solid state sintering for 316 L stainless steel components. J Mater Proc Tech 177:352–355
Song J, Barriere T, Liu B, Gelin JC, Michel G (2010) Experimental and numerical analysis on sintering behaviours of injection moulded components in 316L stainless steel powders. Powder Metall 53:295–304
Takahashi Y, Ueno F, Nishiguchi K (1988) A numerical analysis of the void shrinkage process controlled by surface diffusion. Acta Metall 36:3007–3018
Tay BY, Liu L, Loh NH, Tor SB, Murakoshi Y, Maeda R (2006) Characterization of metallic micro rod arrays fabricated by _MIM. Mater Char 57:80–85
Tikare V, Braginsky M, Bouvard D, Vagnon A (2010) Numerical simulation of microstructural evolution during sintering at the mesoscale in a 3D powder compact. Comput Mater Sci 48:317–325
Weglewski W, Basista M, Chmielewski M, Pietrzak K (2012) Modelling of thermally induced damage in the processing of Cr-Al2O3 composites. Compos Eng 43:255–264
Wonisch A, Kraft T, Moseler M, Riedel H (2009) Effect of different particle size distributions on solid-state sintering: a microscopic simulation approach. J Am Ceram Soc 92:1428–1434
Yu PC, Li QF, Fuh JYH, Li T, Lu L (2007) Two-stage sintering of nano-sized yttria stabilized zirconia process by powder injection moulding. J Mater Process Technol 192–193:312–318